arXiv:1206.0147v1 [quant-ph] 1 Jun 2012

Nonlinear nanomechanical resonators for quantum optoelectromechanics

S. Rips$^{1)}$, I. Wilson-Rae$^{2),1)}$, and M. J. Hartmann$^{1)}$

$^{1)}$ Technische Universität München, Physik Department, James Franck Str., D-85748 Garching, Germany,

$^{2)}$Friedrich Alexander Universität Erlangen-Nürnberg, Staudtstr. 7, D-91058 Erlangen, Germany

E-mail: `simon.rips@ph.tum.de`,`ignacio.wilson-rae@ph.tum.de`, `michael.hartmann@ph.tum.de`

Abstract. We present a scheme for enhancing the anharmonicity of nanomechanical resonators by subjecting them to inhomogenous electrostatic fields. We show that this approach enables access to a novel regime of optomechanics, where the nonlinearity per quanta of the mechanical motion becomes comparable to the linewidth of the optical cavities employed. In this "resolved nonlinearity regime" transitions between phonon Fock states of the mechanical resonator can be selectively addressed. As one application we show that our approach would allow to prepare stationary phonon Fock states in experimentally realistic devices. Such states are manifestly non-classical as they show pronounced negative Wigner functions. We calculate the mechanical steady state by tracing out the cavity modes in the weak optomechanical coupling limit and corroborate our results by a numerical analysis of the full dynamics including the cavity modes. Finally, we show how the negativity of the stationary states' Wigner function can be read off the output spectrum of a weak resonant probe laser and analyse possible imperfections of the envisioned setup in detail.

PACS numbers: 85.85.+j,42.50.Dv,42.50.Wk,03.65.Ta

1. Introduction

Substantial progress in fabricating high-Q mechanical resonators with high frequencies, as well as recent success in cooling them close to the motional groundstate [1, 2, 3, 4], inaugurate a new research field of manifold fundamental interest [5, 7, 6]. The regime of very low temperature, where a quantum mechanical description predicts only few quanta of mechanical motion, promises potential insight into some fundamental questions of decoherence, as well as various technical applications that use the expected quantum behaviour [8, 9, 10]. Fundamental questions, concerning the border between the classical (macroscopic) and the quantum (microscopic) worlds [11], trigger a natural interest in preparing quantum states of "as large as possible" objects and demonstrating their distinct quantum behaviour by appropriate measurements.

Regarding this major goal, it is important to stress that the dynamics of a purely harmonic quantum system is analogous to its classical dynamics, in the sense that expectation values of observables follow the classical equations of motion [12]. Therefore, it is a common approach to introduce nonlinearities in a quantum system in order to detect quantum behaviour. While there is the possiblity to go to the strong optomechanical coupling regime [13, 14, 15] and make use of the nonlinear nature of the standard optomechanical coupling, or to couple to a nonlinear ancilla system [2, 6, 16], we use here a different approach: We introduce a novel kind of optoelectromechanical system that features a tunable *mechanical* nonlinearity. This nonlinearity originates from intrinsic elastic properties [17, 18, 19, 20] and is enhanced with the help of electrostatic fields. This has the advantage that the cavity sideband driving technique is preserved, as this only works in a regime where the optomechanical interaction is weak and can be approximated by a linear coupling. The regime of large mechanical nonlinearity then enables new means to control the mechanical motion at the quantum level, if combined with the coupling to a high-Q optical cavity mode.

The intrinsic anharmonicity in the mechanical motion of real world micro- and nanomechanical resonators is usually very small and therefore only relevant in the regime of large oscillation amplitudes. In order to obtain a sufficiently large anharmonicity for displacements at the scale of the quantum mechanical zero point motion, we propose to use electrostatic gradient forces [21]. These forces originate from the dielectric properties of the resonator material inside a inhomogenious, external field. They can be used to effectively reduce the resonator's stiffness and therefore its resonance frequencies. In turn, this has the effect that the zero point deflection is enhanced up to an extend that the nonlinear contribution becomes important.

Using this technique, the nonlinearity per phonon can be made comparable to the linewidth of a high finesse cavity. This "resolved nonlinearity regime" enables to selectively transfer population from phonon Fock state $|n\rangle$ to $|n+1\rangle$ ($|n'\rangle$ to $|n'-1\rangle$) by driving the spectral line corresponding to n (n') phonons in the blue (red) sideband. While the optomechanical technique of driving sideband transitions is well known from sideband cooling [22, 23], the anharmonicity of the mechanical motion is a new and crucial feature of our approach.

In this paper, we explicitly derive the fundamental mode properties of a nonlinear mechanical resonator subject to the aforementioned gradient forces to obtain a suitable model for the mechanical degree of freedom. Using that model, we analyze the effect of several laser driven cavity modes that are each coupled to the resonator. This enables the identification of parameters that lead to distinct nonclassical steady states.

To demonstrate the capabilities of our scheme, we show results that have been calculated considering state of the art experimental components. For the mechanical resonator we assume a carbon nanotube (CNT) that is mounted on a chip, together with electrodes that generate the electrostatic field. This forms a nanoelectromechanical system (NEMS) based on existing devices. For the cavity we consider a high finesse toroidal or fibre based microcavity which couples to the CNT via its evanescent field.

The remainder of the paper is organized as follows. In section 2 we describe the nonlinear dynamics of thin rods starting from elasticity theory and derive the resulting fundamental mode Hamiltonian. In section 3 we describe our approach to enhance the intrinsic mechanical nonlinearity by mode softening with gradient forces. After that we introduce the optomechanical model with several laser driven cavity modes in section 4. In section 5 a reduced master equation (RME) for the mechanical motion is derived, followed by an analysis of its steady state in section 6. We present numerical results in section 7 and in section 8 we propose a method to measure the mechanical state in an experiment. Finally, we quantitatively discuss central physical properties of our setup, namely the optomechanical coupling mechanicsm in section 9, as well as potential additional photon losses introduced by the employed electrodes in section 10.

2. Elasticity and fundamental mode description for nanoresonators

The harmonic description of the motion of thin rods is based on only considering the bending energy for small deflections [24]. We consider here thin rods, which means that the cross-sectional dimensions, such as the radius for circular cross sections or width and depth for rectangular cross sections, are much smaller than the length L. We also consider the rod to be homogeneous along the longitudinal axis, here parametrized by $x \in \{0, L\}$, with constant mass line density μ and use thin rod elasticity. The planar deflection in the transverse direction is described by a field $y(x)$ where the end points at $x = 0$ and $x = L$ are fixed, i.e. $y(0) = y(L) = 0$. The Lagrangian within this approximation reads

$$\mathcal{L}(y(x,t)) = \frac{\mu}{2}\int \mathrm{d}x\dot{y}^2 - V_{\mathrm{b}}[y(x)]\,, \tag{1}$$

with a kinetic part as well as the bending energy

$$V_{\mathrm{b}}[y(x)] = \frac{1}{2}\int \mathcal{F}\kappa^2 (y'')^2 \mathrm{d}x\,. \tag{2}$$

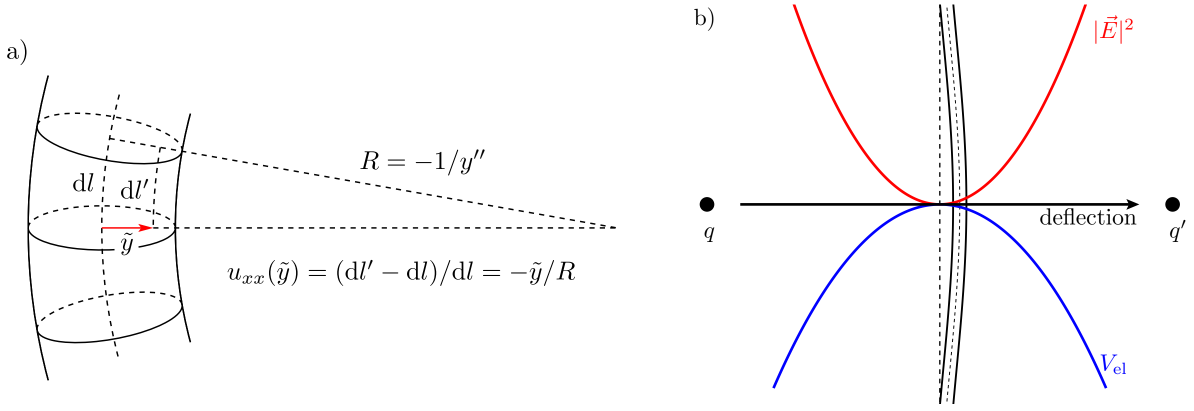

Figure 1. Sketch of the deflected rod. a): The local strain u_{xx} is given by the distance to the elastic line $\tilde{y}$ as well as the local curvature y'' and determines the energy density $\mathrm{d}E/\mathrm{d}V=\frac{1}{2}Yu_{xx}^2$. b) Resonator with electrodes modeled by point charges q,q'. The field profile (red) leads to an inverted parabola for the dielectric potential (blue) around the equilibrium position.

Here, $\mathcal{F}=YA$ is the linear modulus of the rod given by the Young modulus Y of the material times the cross-section area A. $\kappa^2=\frac{1}{A}\int_{\mathrm{cross}}\tilde{y}^2\mathrm{d}A$ is the ratio of bending to compressional rigidity and depends on the cross-sectional geometry, where $\tilde{y}$ is the in-plane coordinate within the cross-section that is directed along the deflection, with origin at the neutral line. For a rectangular cross-section of thickness d, $\kappa=d/\sqrt{12}$, whereas for a circular cross-section with radius R, $\kappa=R/2$. For a cylindrical shell like a nanotube, one finds $\kappa=R/\sqrt{2}$. The energy (2) results from the fact that for small curvature y'', the local strain inside the rod is linear with respect to the distance $\tilde{y}$ to the neutral line (see FIG. 1), while the free energy density is quadratic with respect to the strain. The Lagrangian (1) leads to the equation of motion

$$\mu\ddot{y}+\mathcal{F}\kappa^2y^{(4)}=0\,, \tag{3}$$

where $y^{(4)}$ denotes the 4-th derivative with respect to x. As this equation is linear in y and its derivatives, it leads to harmonic dynamics. The implementation introduced later is best decribed by clamped boundary conditions $y'(0)=y'(L)=0$ for the rod. In that case (3) has the eigenmodes

$$\phi_n(x)=\frac{1}{C_n}\left[\frac{\sin(\nu_nx/L)-\sinh(\nu_nx/L)}{\sin(\nu_n)-\sinh(\nu_n)}-\frac{\cos(\nu_nx/L)-\cosh(\nu_nx/L)}{\cos(\nu_n)-\cosh(\nu_n)}\right], \tag{4}$$

with frequencies $\omega_n=c_{\mathrm{s}}\kappa\left(\nu_n/L\right)^2$, where $c_{\mathrm{s}}=\sqrt{\mathcal{F}/\mu}$ is the phase speed of compressional phonons along the rod. The ν_n are the roots of the transcendental equation $\cos\left(\nu_n\right)\cosh\left(\nu_n\right)=1$, i.e. $\nu_1=4.73$. The C_n are normalization constants chosen such that $\mathbf{max}\left\{\phi_n(x)\right\}=1$. We choose this normalization so that the coefficients in a mode expansion repesent the maximum amplitudes of the deflection associated to each mode. Introducing now the canonical momentum $\Pi(x,t)=\delta\mathcal{L}/\delta\dot{y}(x,t)$, as well as the expansion of the field into the modes

$$y(x,t)=\sum_n \phi_n(x)\mathcal{X}_n(t)\,, \tag{5}$$

yields the Hamilton function of a harmonic oscillator for each mode

$$\mathcal{H}=\sum_n\left(\frac{\mathcal{P}_n^2}{2m_n^*}+\frac{1}{2}m_n^*\omega_n^2\mathcal{X}_n^2\right) \tag{6}$$

with the deflection $\mathcal{X}_n$ and mode momentum $\mathcal{P}_n = m_n^*\partial_t\mathcal{X}_n$ for the n-th mode, as well as the effective mode masses $m_n^* = \mu\int_0^L \phi_n^2(x)\mathrm{d}x$. Corrections to this harmonic description that lead to nonlinearities originate from a streching effect that occurs due to the deflection if the end points of the rod are fixed in space [25]. The resulting strain leads to an additional energy

$$\frac{\mathcal{F}}{2}\frac{(L_t-L)^2}{L}\approx\frac{\mathcal{F}}{8L}\left(\int\mathrm{d}x(y')^2\right)^2\,, \tag{7}$$

where the stretched length is $L_t=\int\sqrt{1+(y')^2}\mathrm{d}x\approx L+\frac{1}{2}\int\mathrm{d}x(y')^2$ with L being the zero deflection length. Including this streching energy leads to a nonlinear extension of the Hamiltonian for the fundamental mode

$$H=\frac{\mathcal{P}^2}{2m^*}+\frac{1}{2}m^*\omega_{\mathrm{m},0}^2\mathcal{X}^2+\frac{\beta}{4}\mathcal{X}^4\,, \tag{8}$$

where we introduced the fundamental frequency $\omega_{\mathrm{m},0}$ and the effective mass of the fundamental mode $m^*\approx 0.3965\,\mu L$. The anharmonicity is given by

$$\beta=\frac{\left(\int_0^1\phi'^2(xL)\mathrm{d}x\right)^2}{\nu_1^4\,(m^*/m)}m^*\omega_{\mathrm{m},0}^2\kappa^{-2}\approx 0.060\,m^*\omega_{\mathrm{m},0}^2\kappa^{-2}\,. \tag{9}$$

The nonlinearity also induces a weak coupling between modes that can be neglected for low enough temperatures. We quantize the Hamiltonian (8) by introducing bosonic mode operators $b^\dagger, b$ given by

$$b=\frac{1}{2}\left(\sqrt{\frac{m^*\omega}{\hbar}}\mathcal{X}+\mathrm{i}\sqrt{\frac{1}{\hbar m^*\omega}}\mathcal{P}\right)\,, \tag{10}$$

and obtain the phononic description

$$H=\hbar\omega_{\mathrm{m},0}b^\dagger b+\hbar\frac{\lambda_0}{2}\left(b^\dagger+b\right)^4\,, \tag{11}$$

with the nonlinearity parameter $\lambda_0=\frac{\beta}{2}x_{\mathrm{ZPM}}^4/\hbar$, where $x_{\mathrm{ZPM}}=\sqrt{\hbar/2m^*\omega_{\mathrm{m},0}}$ is the zero point motion amplitude of the mode. Here, the frequencies $\omega_{\mathrm{m},0}$ and λ_0 refer to fundamental mode properties that result only from the intrinsic elastic forces and without applying any external forces to the rod. As we will describe in the next section, external forces can be used to tune the resonance frequency $\omega_{\mathrm{m},0}\rightarrow\omega_{\mathrm{m}}$, which will in turn change x_{ZPM} and $\lambda_0\rightarrow\lambda$.

3. Enhanced nonlinearity by mode softening

As stated above, the nonlinearity per phonon scales as $\lambda \propto x_{\mathrm{ZPM}}^4 \propto \omega_{\mathrm{m}}^{-2}$. Therefore, we intend to lower the harmonic frequency $\omega_{\mathrm{m},0}$ by applying external forces. One way to change the mode frequency that has been discussed previously, is to add an additional external force along the rod axis, that causes compressive or tensile strain [25, 26]. An alternative approach, that promises better control but yields the same potential for the fundamental mode, is to use a static electric field that is strongly inhomogenious in the direction of deflection. If the rod material shows suitable dielectric properties, this produces an additional, inverted square potential with respect to the deflection, see FIG. (1b). To describe our approach we consider tip electrodes with suitable potentials at each side of the nanoresonator that generate a static field. In our calculation we model the electrodes by point charges q, q'. The electrostatic energy associated to the dielectric per unit length along the rod can be described by

$$W(x,y) = -\frac{1}{2}[\alpha_{\parallel} E_{\parallel}^2(x,y) + \alpha_{\perp} E_{\perp}^2(x,y)]\,, \tag{12}$$

where x, y are the co-ordinates along the resonator axis and the direction of its deflection. $E_{\parallel,\perp}$ are external field components parallel and perpendicular to the beam axis and $\alpha_{\parallel,\perp}$ the respective screened polarizabilities. We can expand $W(x,y)$ to second order in the displacement y and get an additional contribution to the Hamiltonian that reads

$$V_{\mathrm{el}} = V_{\mathrm{el}}^{(1)} + V_{\mathrm{el}}^{(2)} = \int_0^L \left.\frac{\partial W(x,y)}{\partial y}\right|_{y=0} y(x)\mathrm{d}x + \frac{1}{2}\int_0^L \left.\frac{\partial^2 W(x,y)}{\partial y^2}\right|_{y=0} y^2(x)\mathrm{d}x\,, \tag{13}$$

where we dropped the displacement independent constant $W(x,0)$ which is irrelevant for the dynamics. Inserting the modes (5) we get

$$V_{\mathrm{el}} = \sum_n F_n \mathcal{X}_n + \frac{1}{2}\sum_{lk} W_{lk}\mathcal{X}_l\mathcal{X}_k\,, \tag{14}$$

with $F_n = \int \partial_y W|_{y=0}\,\phi_n \mathrm{d}x$ and $W_{lk} = \int \partial_y^2 W|_{y=0}\,\phi_l\phi_k \mathrm{d}x$. The electrostatic forces F_n cause a static deflection of the rod and shift it's equilibrium position. However if the rod interacts with the photon fields of a nearby cavity, those fields will also cause a deflecting force. For convenience we choose parameters such that these two forces compensate and the equilibrium position remains unshifted (see section 4).

In general, the contributions of W_{lk} will cause weak interactions between the modes, as W_{lk} is not a diagonal matrix. By diagonalizing the Hamiltonian of the rod in the presence of electrostatic fields, one can find new mormal modes. For the parameters considered in this work, the induced corrections to the mode shapes are however found to be negligibly small. We thus end up with the a mechanical Hamiltonian for the fundamental mode of the form,

$$H_{\mathrm{m}} = \frac{\mathcal{P}^2}{2m^*} + \frac{1}{2}m^*\omega_{\mathrm{m}}^2\mathcal{X}^2 + \frac{\beta}{4}\mathcal{X}^4 + F_0\mathcal{X}\,, \tag{15}$$

with a reduced frequency $\omega_{\mathrm{m}}^2 \approx \omega_{\mathrm{m},0}^2 - |W_{00}|/m^*$. In a phononic description this reads

$$H_{\mathrm{m}} = \hbar\omega_{\mathrm{m}} b^\dagger b + \hbar\frac{\lambda}{2}(b^\dagger + b)^4 + F_0 x_{\mathrm{ZPM}}(b^\dagger + b)\,, \tag{16}$$

where the nonlinearity per phonon λ is now increased by a factor $\zeta^2 = (\omega_{\mathrm{m},0}/\omega_{\mathrm{m}})^2$.

4. Optomechanical Model

We consider a typical optomechanical setup with a micro toroid cavity coupled to the nanomechanical resonator, where the displacement of the latter modifies the frequencies of the cavity modes. The cavity modes with frequencies ω_i that contribute to the dynamics are described by creation and annihilation operators ${a_i}^\dagger$ and a_i. They are each driven by a classical laser of input power P_i and frequency $\omega_{\mathrm{L},i}$. The coupling strength to the different cavity modes is given by $G_{0,j} x_{\mathrm{ZPM}}$, where $G_{0,j} = \frac{\partial \omega_j}{\partial \mathcal{X}}$ is the optical frequency shift per deflection deflection $\mathcal{X}$. Thus, in a frame rotating with the laser field modes, the Hamiltonian describing the coupled system reads ($\hbar \to 1$)

$$H = \sum_j \left[\frac{\Omega_j}{2}\left(a_j^\dagger + a_j\right) - \Delta_j {a_j}^\dagger a_j + G_{0,j} x_{\mathrm{ZPM}} {a_j}^\dagger a_j \left(b^\dagger + b\right) \right] + H_{\mathrm{m}}. \tag{17}$$

Here we have introduced the laser detunings denoted by $\Delta_j = \omega_{\mathrm{L},j} - \omega_j$ and $\Omega_j/2 = \sqrt{P_j \kappa_{\mathrm{ex},j}/\hbar\omega_{\mathrm{L},j}}$, with $\kappa_{\mathrm{ex},j}$ being the cavity decay rates into the associated outgoing electromagnetic modes.

Both the field inside the cavity and the mechanical motion are subject to damping, which in the regime of weak optomechanical coupling, small nonlinearity and low mechanical occupation is well described by a master equation with Lindblad form damping terms. With the decay rate rates for the cavity modes κ_j and the mechanical damping rate γ_{m}, this master equation reads

$$\dot{\rho} = -\mathrm{i}\,[\rho, H] + \sum_j \frac{\kappa_j}{2}\mathcal{D}(a_j)\rho + \frac{\gamma_{\mathrm{m}}}{2}\left[(\overline{n}+1)\mathcal{D}(b)\rho + \overline{n}\mathcal{D}(b^\dagger)\rho\right]\,. \tag{18}$$

Here we introduced the Lindblad form dissipator $\mathcal{D}(\hat{o})\rho = 2\hat{o}\rho\hat{o}^\dagger - \hat{o}^\dagger\hat{o}\rho - \rho\hat{o}^\dagger\hat{o}$, as well as the Bose occupation number $\overline{n} = \left[\exp\left(\frac{\hbar\omega_{\mathrm{m}}}{k_{\mathrm{B}}T}\right) - 1\right]^{-1}$ of the phonon bath mode with frequency ω_{m} at tempertature T. A more precise treatment of the mechanical damping accounts for the fact that, due to the mechanical nonlinearity, there is more than one bath mode resonantly coupling to the mechanical mode. However, for high-Q resonators, (18) proofs to be sufficiently accurate.

As usual, we expand the cavity field operators around their steady state values and adpot a shifted representation $a_j \to a_j + \alpha_j$, with $\alpha_j = \Omega_j/(2\Delta_j + \mathrm{i}\kappa_j)$, in which the master equation has the same form as in (18) but with the shifted system Hamiltonian

$$H' = \sum_j \left[-\Delta_j {a_j}^\dagger a_j + \left(\frac{g_{\mathrm{m},j}^*}{2} a_j + \mathrm{H.c.}\right)\left(b^\dagger + b\right) \right] + \omega_{\mathrm{m}} b^\dagger b + \frac{\lambda}{2}(b^\dagger + b)^4 \tag{19}$$

with $g_{\mathrm{m},j} = 2\alpha_j G_{0,j} x_{\mathrm{ZPM}}$ and where we dropped the nonlinear term $\propto {a_j}^\dagger a_j(b^\dagger + b)$ in the coupling, which is valid for $\langle {a_j}^\dagger a_j\rangle \ll |\alpha|^2$. We also assumed that the static electric fields are chosen such that $F_0 = -\hbar \sum_j G_{0,j}|\alpha_j|^2$, so that the equilibrium position of the mechanical oscillator is undeflected.

5. Reduced Master Equation

As we are interested in the dynamics of the mechanical resonator, we now choose to trace out the cavity degrees of freedom to obtain a reduced master equation for the mechanical motion. To do so, we focus on the parameter regime suitable for back action cooling. Indeed, we will find that the processes leading to nonclassical steady states can be interpretated as a combination of cooling and heating processes with respect to different number state transitions. Successful cooling (or heating) requires $g_{\mathrm{m},j} \ll \kappa_j$ and $\overline{n}\gamma_{\mathrm{m}} \ll g_{\mathrm{m},j}$. The first condition ensures that the cavity modes stay in the vacuum state with respect to the shifted represention. This enables us to trace out the cavity modes safely. The second condition ensures that the influence of the cavity on the mechanical motion is greater than the influence of the thermal environment. We use this separation of frequency scales to adiabatically eliminate the photon degrees of freedom. An outline of this approach is given in appendix refappendix.

For our analysis, we focus on the regime of small nonlinearity $\lambda \ll \omega_{\mathrm{m}}$ and apply a rotating wave approximation (RWA) for the mechanical part $H_{\mathrm{m}} \to H'_{\mathrm{m}}$. This diagonalizes the mechanical Hamiltonian in the number state basis (again assuming $F_0 = -\hbar \sum_j G_0|\alpha_j|^2$)

$$\omega_{\mathrm{m}} b^\dagger b + \frac{\lambda}{2}\left(b^\dagger + b\right)^4 \to \omega'_{\mathrm{m}} b^\dagger b + \frac{\lambda'}{2} {b^\dagger}^2 b^2, \tag{20}$$

with the shifted frequency $\omega'_{\mathrm{m}} = \omega_{\mathrm{m}} + \lambda'$ and $\lambda' = 6\lambda$. Note that in this approximation the energy eigenstates of mechanical motion are Fock number states. It is useful to switch to an interaction picture with respect to the nonlinear mechanical mode which requires to write the mechanical mode operator b in its matrix representation in the Fock basis, $b_n = \sqrt{n}|n-1\rangle\langle n|$, as those projectors rotate at frequencies that now depend on the Fock number n,

$$b = \sum_n \sqrt{n}|n-1\rangle\langle n| \to \sum_n \mathrm{e}^{-\mathrm{i}\delta_n t} b_n\,, \tag{21}$$

with $\delta_n = \omega'_{\mathrm{m}} + \lambda'(n-1)$. This Fock number resolved dynamics consequently appears in the resulting reduced master equation for the mechanical density operator $\mu = \mathrm{Tr_c}\left\{\rho\right\}$

$$\begin{aligned}\dot{\mu} = & -\mathrm{i}\left[\omega'_{\mathrm{m}} b^\dagger b + \frac{\lambda'}{2} b^\dagger b^\dagger b b + \sum_{n,j}\left(\Delta^{n,+}_{\mathrm{m},j} b^\dagger_n b_n + \Delta^{n,-}_{\mathrm{m},j} b_n b^\dagger_n\right), \mu\right] + \\ & + \frac{1}{2}\sum_n \left\{\left[\sum_j A^n_{-,j} + \gamma_{\mathrm{m}}\left(\overline{n}+1\right)\right]\mathcal{D}(b_n)\mu + \left[\sum_j A^n_{+,j} + \gamma_{\mathrm{m}}\overline{n}\right]\mathcal{D}(b^\dagger_n)\mu\right\},\end{aligned} \tag{22}$$

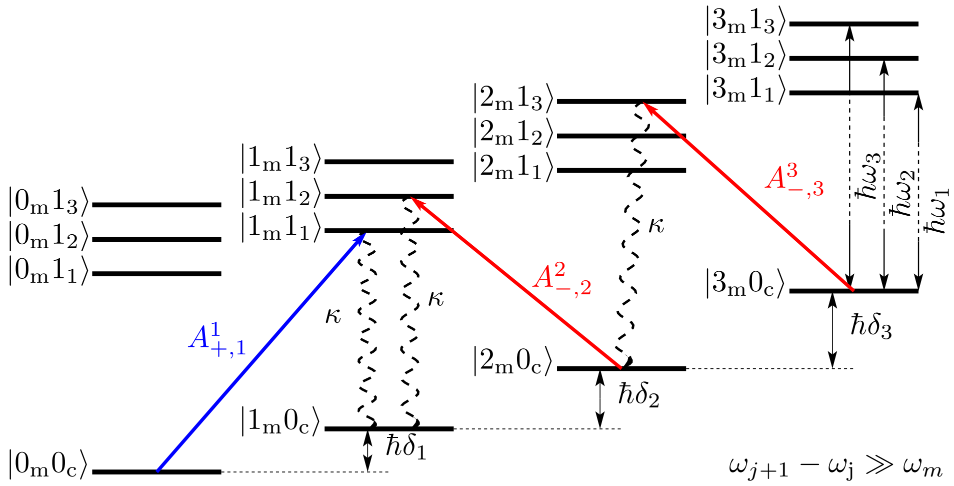
$|0_\mathrm{m}1_3\rangle$
$|0_\mathrm{m}1_2\rangle$
$|0_\mathrm{m}1_1\rangle$
$|0_\mathrm{m}0_\mathrm{c}\rangle$
$|1_\mathrm{m}1_3\rangle$
$|1_\mathrm{m}1_2\rangle$
$|1_\mathrm{m}1_1\rangle$
$|1_\mathrm{m}0_\mathrm{c}\rangle$
$|2_\mathrm{m}1_3\rangle$
$|2_\mathrm{m}1_2\rangle$
$|2_\mathrm{m}1_1\rangle$
$|2_\mathrm{m}0_\mathrm{c}\rangle$
$|3_\mathrm{m}1_3\rangle$
$|3_\mathrm{m}1_2\rangle$
$|3_\mathrm{m}1_1\rangle$
$|3_\mathrm{m}0_\mathrm{c}\rangle$
$A^1_{+,1}$
$A^2_{-,2}$
$A^3_{-,3}$
κ
κ
κ
$\hbar\delta_1$
$\hbar\delta_2$
$\hbar\delta_3$
$\hbar\omega_3$
$\hbar\omega_2$
$\hbar\omega_1$
$\omega_{j+1}-\omega_\mathrm{j} \gg \omega_m$

Figure 2. Level diagram of the coupled cavity-resonator-system. $|n_\mathrm{m}n'_j\rangle$ denotes a state with n phonons and n' photons in the cavity mode j while the other cavity modes are in the vacuum state. $|n_\mathrm{m}0_\mathrm{c}\rangle$ means all cavity modes are in the groundstate (empty). Due to the nonlinearity, the mechanical energy level spacings depend on the fock number n and can be addressed individually. Here we have sketched the driving of the phonon transition $|0\rangle \rightarrow |1\rangle$ by a blue detuned laser $\Delta_1 = \omega_{\mathrm{L},1} - \omega_1 = \delta_1$ as well as those of transitions $|2\rangle \rightarrow |1\rangle$ and $|3\rangle \rightarrow |2\rangle$ by red detuned lasers $\Delta_2 = -\delta_2$, $\Delta_3 = -\delta_3$.

where we have introduced small cavity induced frequency shifts for the nanoresonator

$$\Delta^{n,\pm}_{\mathrm{m},j} = \frac{g^2_{\mathrm{m},j}\,(\Delta_j \pm \delta_n)}{4(\Delta_j \pm \delta_n)^2 + \kappa_j^2}\,, \tag{23}$$

as well as the transition rates $A^n_{\pm,j}$. The latter are exact analogues to the cooling and heating rates recovered in [27] and are here given by

$$A^n_{\pm,j} = g^2_{\mathrm{m},j}\frac{\kappa_j}{4(\Delta_j \mp \delta_n)^2 + \kappa_j^2}\,. \tag{24}$$

In the context of cooling, the analog rates determine the effective temperature of the cavity modes as a cool bath and so also the final temperature of the mechanical resonator. Here, in contrast, the influence of the $A^n_{\pm,j}$ is focussed on driving transitions between mechanical Fock states $|n\rangle$ and $|n-1\rangle$, where the direction of the drive is given by the + or − sign. The magnitude of $A^n_{\pm,j}$ as a function of the detuning Δ_j is a Lorentzian with resonance $\pm\delta_n$ and width κ_j. This enables to selectively address specific transitions by choosing the detuning of one of the lasers to match the corresponding energy spacing. In figure 2, a sketch of this mechanism is given using the relevant energy level diagram.

6. Steady state solution

We assume that the density matrix μ will be diagonal in steady states and seek for a solution of (22) with the ansatz

$$\mu = \sum_n P_n |n\rangle\langle n| \,. \tag{25}$$

Since within this ansatz the unitary part vanishes, this yields the steady state relations

$$\frac{P_n}{P_{n-1}} = \frac{\sum\limits_j A^n_{+,j} + \gamma_{\mathrm{m}}\overline{n}}{\sum\limits_j A^n_{-,j} + \gamma_{\mathrm{m}}\left[\overline{n}+1\right]} \equiv F(n) \,. \tag{26}$$

These relations together with the normalization $\sum_n P_n = 1$ define the steady state of the mechanical oscillator. It can be calculated numerically by imposing a cutoff number n_0, for which $\sum_{n=n_0+1}^{\infty} P_n \ll 1$, to find P_0 via $1/P_0 = \sum_n^{\infty} \prod_{i=0}^{n-1} F(i+1) \approx \sum_n^{n_0} \prod_{i=0}^{n-1} F(i+1)$ and the other P_n successively with the recursion relation (26). Note that without laser drives the $A^n_{\pm,j}$ vanish and we obtain relations characterising a thermal state at the bath temperature T. If instead we let $\lambda \to 0$, the ratio P_n/P_{n-1} becomes n-independent, implying a thermal state at a different temperature depending on the laser detunings and amplitudes.

7. Setup and results

For the experimental realization we envisage a setup as shown in figure 3, comprising a NEMS chip and a high finesse toroidal micro cavity [29, 30]. The NEMS chip consists of a single-walled CNT ($c_{\mathrm{s}} = 21000\,\mathrm{ms}^{-1}$) acting as the nanoresonator [31, 32], as well as electrodes that generate the softening field. The nanoresonator interacts with the evanescent field of the micro cavity via dielectric gradient force (see section 9). A CNT is a favorable implementation, as the intrinsic nonlinearity per phonon can be found to scale as $\lambda_0 \propto \left(\kappa^2 m\right)^{-1}$, which suggests a small transverse dimension and mass. Furthermore, carbon nanotubes show ultra-low dissipation [33], that is even decreased in the regime of small amplitudes [34].

We calculated the steady state of mechanical motion for several sets of laser detunings Δ_j, both by use of the relations (26) and by solving the full master equation (18) with the shifted system Hamiltonian (19). In order to obtain self consistency with respect to the applyied RWA (20) on the analytical side, as well as justification for a Fock number cutoff in the numerical treatment, we aim to produce steady states with small phonon occupations $\langle b^\dagger b\rangle \sim 1$. We also want to produce states with a significant negativity in the Wigner phase-space distribution, as this is a commonly accepted indicator of a nonclassical state. Therefore, the most promising choice is to aim at a single phonon Fock state $|1\rangle$ [35]. This state's Wigner distribution shows

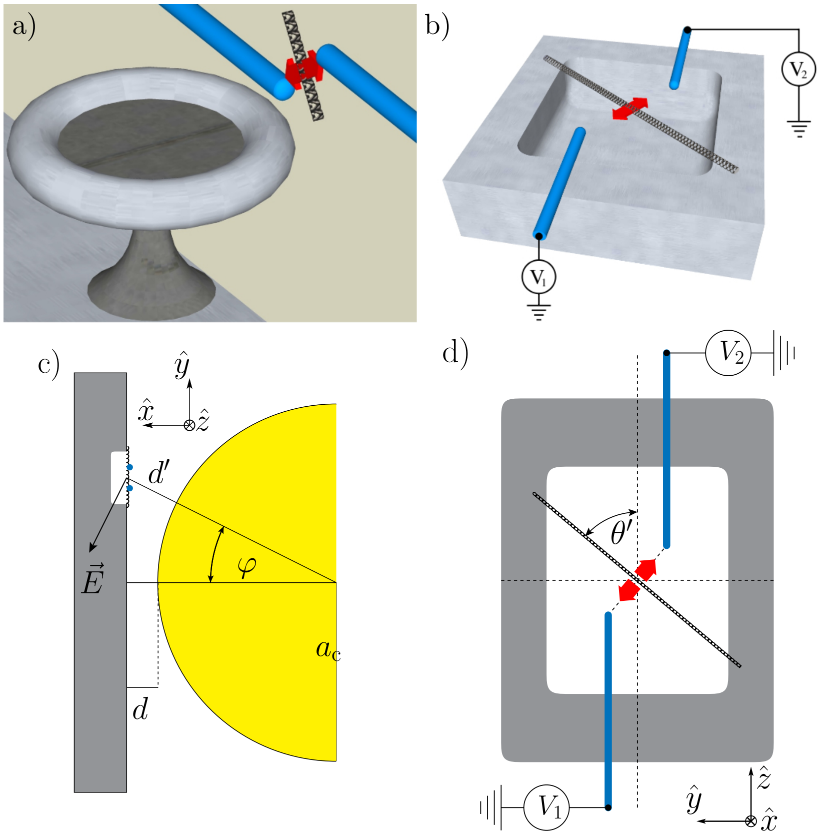

Figure 3. a): Micro toroid cavity with nearby CNT (not to scale). b): NEMS-chip with CNT-resonator and electrodes. c) Schematic top view of the NEMS chips with the CNT oscillating in the $\hat{z}$-$\hat{y}$-plane. d): Schematic cross-sectional view of the NEMS-Chip and the cavity rim (yellow). The NEMS-chip is mounted in the evanescent cavity field at a distance d to the cavity rim surface. The nanoresonator is displaced from the closest point to allow for an optomechanical coupling that is linear in the resonator's deflection.

a negativ peak of depth $W(0,0) = -2/\pi$ at the origin of the phase-space, which is the maximum negativity attainable for physical quantum states. In order to drive the nanoresonator to this state, the plausible strategy is to drive the Fock state transitions $|0\rangle \rightarrow |1\rangle$, $|2\rangle \rightarrow |1\rangle$ as well as $|3\rangle \rightarrow |2\rangle$ to obtain net cooling. This is done by choosing laser detunings $\Delta_1 = \delta_1$ and $\Delta_{2,3} = -\delta_{2,3}$, repectively. In figure (4) we show results for this scenario, comprising to different sets of parameters.

The system parameters considered in figure 4a), b) can for example be realized with a (10,0)-CNT of length $L = 1$ μm and radius $R = 0.39$ nm, that is softened by a factor $\zeta = 4.0$. The polarisability of the CNT is $\alpha_{||} = 143\left(4\pi\epsilon_0\text{Å}^2\right)$, $\alpha_{\perp} = 10.9\left(4\pi\epsilon_0\text{Å}^2\right)$ [36] and for an electrode tip distance of 20 nm from the resonators axis, we find for the maximum fields at the axis $E_{||} \approx 1.20 \cdot 10^7$ V/m and $E_{\perp} \approx 1.78 \cdot 10^6$ V/m. The cavity is a silica ($n_c = 1.44$) microtoroid with wavelength $2\pi c/\omega_j \approx 1.1$ μm, circumference $L_c = 1.3$ mm and finesse $\mathcal{F}_c = 3 \cdot 10^6$ [37]. With an optical mode volume $V_{\text{mode}} = 4.0 \cdot 10^{-15}$ m^3 and an decay length of the evanescent field $k_{\perp}^{-1} \approx 0.17$ μm, the

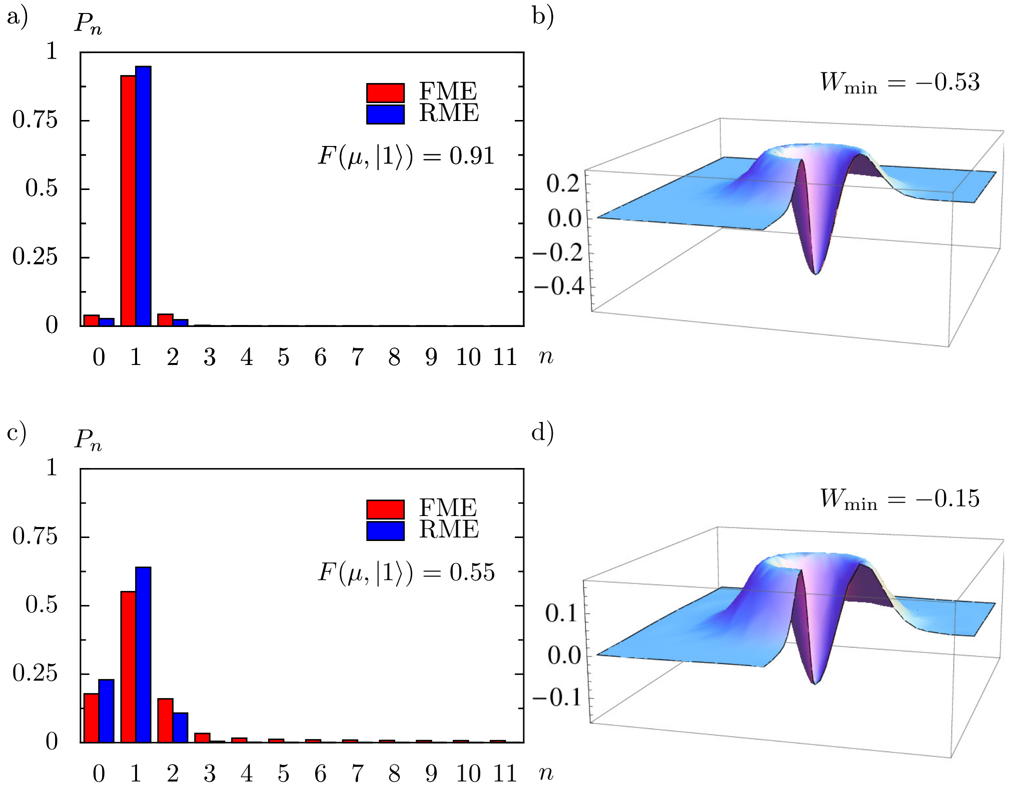

Figure 4. Steady state results for the given effective paramters, comparing results for the reduced master equation (RME) and full master equation (FME). The given fidelities F and the Wigner representation correspond to the FME results. Plots a),b): $\omega_{\mathrm{m}}/2\pi = 5.23$ MHz, $\lambda'/2\pi = 104$ kHz, $g_j/2\pi = 20.9$ kHz, $\kappa_j/2\pi = 52.3$kHz. The ambient temperature is $T = 20$ mK and $Q_{\mathrm{m}} = 5 \cdot 10^6$. Plots c),d): $\omega_{\mathrm{m}}/2\pi = 2.13$ MHz, $\lambda'/2\pi = 42.7$ kHz, $g_j/2\pi = 12.8$ kHz, $\kappa_j/2\pi = 64.2$kHz, $T = 30$ mK and $Q_{\mathrm{m}} = 1.5 \cdot 10^6$.

given coupling strength can be reached by placing the NEMS chip at distance $d = 50$ nm from the cavity rim and with a launched input power $P_{\mathrm{in},j} = 0.14$ W for each laser (assuming $\kappa_{\mathrm{ex}}/\kappa = 0.1$).

In turn for example 4c), d) we have $L = 1.7$ µm and $\zeta = 3.3$ which corresponds to $E_{||} \approx 5.3 \cdot 10^6$ V/m and $E_{\perp} \approx 1.0 \cdot 10^6$ V/m, as well as $L_{\mathrm{c}} = 1.80$ mm, $\mathcal{F}_{\mathrm{c}} = 2 \cdot 10^6$, $V_{\mathrm{mode}} = 5.5 \cdot 10^{-15}$ m^3 and $P_{\mathrm{in},j} = 2.6$ mW. Here, we also assumed a decrease of the mechanical Q by the softening about a factor ζ to $Q = 1.5 \cdot 10^6$.

Of course, the presented scheme also allows for the preparation of other Fock states, or mixtures of Fock states. A few examples are given in figure 5.

8. Measurement via output power spectrum

The steady state of the nanoresonator can be probed with an additional laser, weakly driving one cavity mode on resonance, i.e. $\Delta = 0$. This mode has to be distinct from the modes used for the state preparation. Then, the occupation of different Fock states

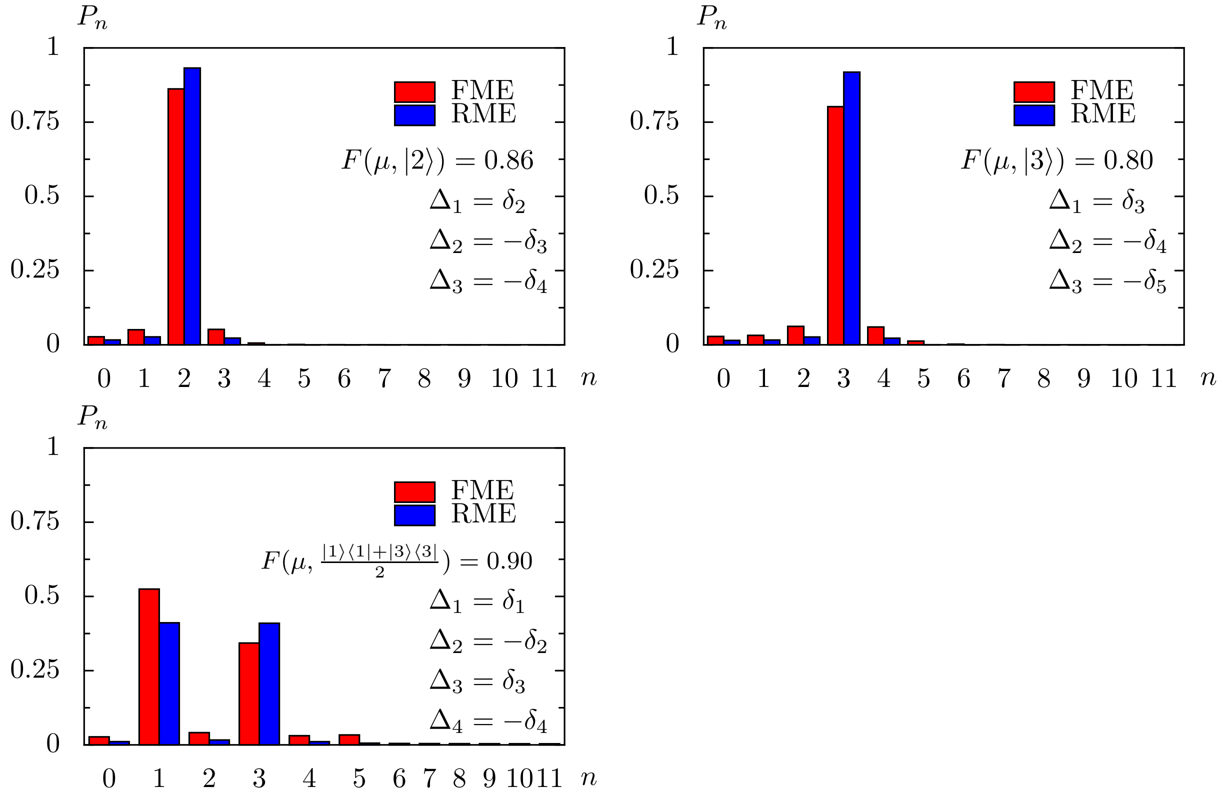

Figure 5. Steady states for a nanoresontor with the parameters given in figure 4a), b) and different sets of laser detunings Δ_j.

can be extracted from the sideband structure in the power spectrum

$$S(\omega) = \frac{1}{2\pi} \int_{-\infty}^{\infty} \mathrm{d}\tau \mathrm{e}^{-\mathrm{i}(\omega-\omega_\mathrm{L})\tau} \langle {a_\mathrm{out}}^\dagger(t+\tau) a_\mathrm{out}(\tau) \rangle_\mathrm{SS} \,. \tag{27}$$

The output field $a_\mathrm{out}(t)$, is related to the intra cavity field $a(t)$ via the standard input-output relation [38], $a_\mathrm{out} = \sqrt{\kappa_\mathrm{ex}} a + a_\mathrm{in}$, while the dynamics of the intra cavity field can be described by a quantum Langevin equation

$$\dot{a} = -\frac{\kappa}{2} a - \mathrm{i} G_0 x_\mathrm{ZPM} \left(b^\dagger + b \right) (a + \alpha) + \sqrt{\kappa_\mathrm{ex}} \delta a_\mathrm{in}(t) + \sqrt{\kappa - \kappa_\mathrm{ex}} \delta c_\mathrm{in}(t) \,, \tag{28}$$

where δa_in, δc_in are the fluctuations of the input field in the laser mode and the other bath modes. Defining $a^{(0)}$ to be a solution for $G_0 = 0$, we can integrate (28) formally and apply a Dyson series type expansion to first order in the coupling strength per photon, $G_0 x_\mathrm{ZPM}$, to find for the motion of the cavity modes

$$\begin{aligned} a(t) &\approx a^{(0)}(t) - \mathrm{i} G_0 x_\mathrm{ZPM} \int_0^t \mathrm{d}\tau \mathrm{e}^{-\kappa/2(t-\tau)} \left[b^\dagger(\tau) + b(\tau) \right] \left[a^{(0)}(\tau) + \alpha \right] \\ &\approx a^{(0)}(t) - \mathrm{i} \frac{g_\mathrm{m}}{2} \sum_n \left[\frac{b_n(t)}{\mathrm{i}\delta_n + \kappa/2} + \mathrm{H.c.} \right] \end{aligned} \tag{29}$$

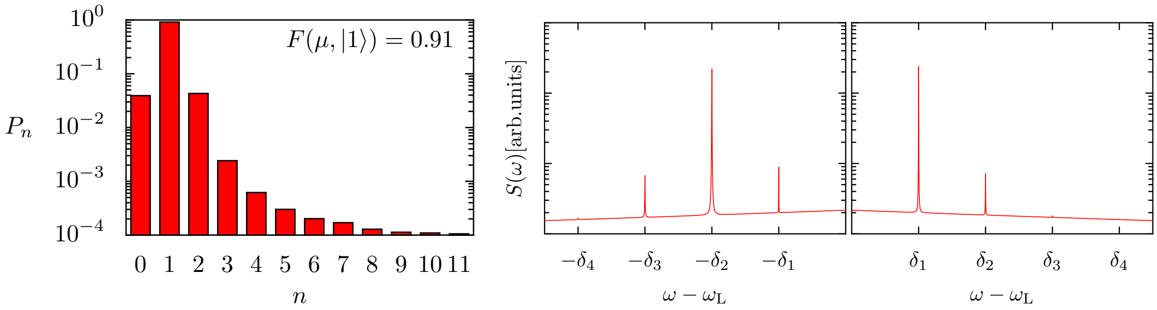

Figure 6. Left: Example result. Right: Corresponding output spectrum around the upper and lower sideband of a resonant driving laser. The peaks correspond to different diagonal entries of the mechanical density matrix. They are separated by λ'. The relative weights of Stokes and anti-Stokes peaks reflect the ratios P_n/P_{n-1}.

Here, the contribution of the fluctuations is included in the free field solution $a^{(0)}(t)$ and the input field operators have already been written in a shifted represention $a_{\rm in}(t)\rightarrow\delta a_{\rm in}(t)+\langle a_{\rm in}\rangle$,, which splits off the coherent part of the input.

The spectrum consists of a contribution at the laserline $\omega=\omega_{\rm L}$, as well as a sideband structure due to the interaction with the mechanical mode. We concentrate on the contributions to the sidebands, which to lowest order in $g_{\rm m}/\omega_{\rm m}$ are given by the first order two-time correlations of the mechanical motion. The latter can be calculated with help of the reduced master equation (22) and by use of the quantum regression theorem. The only nonvanishing contributions in the steady state are $\langle b_n^\dagger(t+\tau)b_n(t)\rangle_{\rm SS}={\rm e}^{[{\rm i}\delta_n-\gamma_{\rm eff}^n/2]\tau}nP_n$ and $\langle b_n(t+\tau)b_n^\dagger(t)\rangle_{\rm SS}={\rm e}^{[-{\rm i}\delta_n-\gamma_{\rm eff}^n/2]\tau}nP_{n-1}$, where we neglected the contributions of the $\Delta_{\rm m}^{n,\pm}$ as they induce only a small shift of the peak positions. Using $\langle A(t-\tau)B(t)\rangle=\langle A(t+\tau)B(t)\rangle^*$ we finally obtain

$$S(\omega\neq\omega_{\rm L})=\frac{\kappa_{\rm ex}}{8\pi}\sum_n\frac{|g_{\rm m}|^2}{\delta_n^2+\kappa^2/4}\left[\frac{n\gamma_{\rm eff}^nP_{n-1}}{[\delta\omega+\delta_n]^2+\frac{\gamma_{\rm eff}^{n\,2}}{4}}+\frac{n\gamma_{\rm eff}^nP_n}{[\delta\omega-\delta_n]^2+\frac{\gamma_{\rm eff}^{n\,2}}{4}}\right], \tag{30}$$

with $\delta\omega=\omega-\omega_{\rm L}$, the distance from the input frequency. Hence the spectrum shows Lorentzian peaks, separated by frequencies δ_n that match the mechanical energy level spacings from the laser line. The linewidth of the peaks is given by $\gamma_{\rm eff}^n=n\left\{A_-^n+A_+^n+\gamma_{\rm m}\left[2\overline{n}+1\right]\right\}+(n-1)\left\{A_-^{n-1}+\gamma_{\rm m}\left[\overline{n}+1\right]\right\}+(n+1)\left\{A_+^{n+1}+\gamma_{\rm m}\overline{n}\right\}$, which satisfies $\gamma_{\rm eff}^n\ll\lambda$ for small Fock numbers n provided that $\overline{n}\gamma_{\rm m}\ll g_{\rm m}$. Making use of expression (30), the ratios P_n/P_{n-1} can be measured by comparing integrated peak intensities $I(\omega)$ at positions $\omega-\omega_{\rm L}=\pm\delta_n$ as

$$\frac{I(\omega_{\rm L}+\delta_n)}{I(\omega_{\rm L}-\delta_n)}=\frac{P_n}{P_{n-1}}\,. \tag{31}$$

These ratios need to be measured up to a Fock number n_0 above which the spectral lines become invisible indicating that the occupations probabilities P_n become vanishingly small. Here, the stationary nature of the motional states considerably simplifies their measurement as compared to phonon Fock states that might be prepared by projective measurements [39, 40, 41].

In the following two sections we analyze important practical aspects of the envisioned implementation with a carbon nanotube coupled to a toroidal microcavity in more detail. Readers who are only interested in the results of the discussed mechanism may thus directly turn to the conclusions section.

9. Optomechanical coupling via the evanescent field

In this section we derive an estimate for the coupling between the mechanical displacement and the cavity field. The coupling arises as the energy of the dielectric oscillator in the evanescent electric field depends on the field strength at the location of the oscillator. As the evanescent field decays with distance to the cavity rim, altering the oscillator-cavity distance by displacing the oscillator results in a change of energy. Thus, the coupling part of the Hamiltonian is given by the dielectric energy

$$H_{\mathrm{c}} = -\frac{1}{2}\int_V \vec{P}(\vec{r})\cdot\vec{E}(\vec{r}) \tag{32}$$

where the polarization is $\vec{P}(\vec{r}) = \overleftrightarrow{\alpha}\cdot\vec{E}(\vec{r})$ with $\overleftrightarrow{\alpha}$ the screened polarizability tensor and $\vec{E}$ the external field. The integration is taken over the oscillator volume.

Given the dimensions of the microcavity, the cavity rim can be locally modeled by a straight, cylindrical fiber. We introduce cylindrical coordinates (r, ϕ, z) with the $\hat{z}$-direction along the fiber axis (compare FIG. 3c) and consider $\mathrm{TE}_{0,n}$ modes, as a transverse electric field is advantageous with repect to possible losses that are discussed in section 10. The corresponding transverse fields are given by [42]

$r < a_{\mathrm{c}}$:

$$B_r = -\mathrm{i}\frac{k_{||}}{\gamma^2}\frac{\partial B_z}{\partial r}\,, \tag{33}$$

$$E_{\varphi} = -\frac{\omega}{k_{||}}B_r\,, \tag{34}$$

$r > a_{\mathrm{c}}$:

$$B_r = -\mathrm{i}\frac{k_{||}}{\kappa_{\perp}^2}\frac{\partial B_z}{\partial r}\,, \tag{35}$$

$$E_{\varphi} = -\frac{\omega}{k_{||}}B_r\,, \tag{36}$$

where axial field reads

$$B_z(r,z) = B_z(0)J_0(\gamma r)\mathrm{e}^{\mathrm{i}k_{||}z}\,, \qquad r < a_{\mathrm{c}}\,, \tag{37}$$

$$B_z(r,z) = \tilde{\xi}B_z(0)\frac{K_0^{(1)}(\kappa_\perp r)}{K_0^{(1)}(\kappa_\perp a_{\mathrm{c}})}\mathrm{e}^{\mathrm{i}k_{||}z}\,, r > a_{\mathrm{c}}\,, \tag{38}$$

with the modified Bessel function $K_0^{(1)}$ and the Bessel function of first kind J_0, and where $\kappa_\perp$ and γ are the transverse wave vectors outside and inside the waveguide, respectively. The ratio of the field maximum inside the waveguide to the field at $r = a_{\mathrm{c}}$ is given by $\tilde{\xi} = B_z(a_{\mathrm{c}})/B_z(0) \approx 0.4$ if $a_{\mathrm{c}}\gamma$ coincides with the first zero of $J_1(x)$, which is $a_{\mathrm{c}}\gamma \approx 3.8$. We further approximate the evanescent electric field for $r > a_{\mathrm{c}}$, using $2\kappa_\perp a_{\mathrm{c}} \gg 1$ and assume a frequency well above cutoff, so that $k_{||} \approx n_{\mathrm{c}}k \gg 1/a_{\mathrm{c}}$. With these approximations, the evanescent field can be written

$$E_\varphi(r) \approx -\mathrm{i}\frac{\omega}{\kappa_\perp}\tilde{\xi}B_z(0)\sqrt{\frac{a_\mathrm{c}}{r}}\mathrm{e}^{-\kappa_\perp(r-a_\mathrm{c})}\mathrm{e}^{\mathrm{i}nkz}\,. \tag{39}$$

This field will later be used to estimate losses induced by the electrodes. In order to determine the optomechanical coupling strength, we write the electric field in its quantized form

$$\vec{E}(\vec{r}) = \sqrt{\frac{\hbar\omega_\mathrm{c}}{2\epsilon_0}}(a^\dagger + a)U(r)\hat{\varphi} \quad \text{where} \quad U(r) \approx \frac{1.7}{n_\mathrm{c}\sqrt{V_\mathrm{mode}}}\sqrt{\frac{a_\mathrm{c}}{r}}\xi\mathrm{e}^{-\kappa_\perp(r-a_\mathrm{c})}\,, \tag{40}$$

with photon operators $a, a^\dagger$ and the mode function $U(r)$ for the evanescent part. Here, $V_\mathrm{mode} \approx 0.5\,\pi a_\mathrm{c}^2 L_\mathrm{c}$ is the cavity's optical mode volume and ξ denotes the ratio of the maximum field inside the waveguide to the field at the waveguide surface. The zero point motion x_ZPM of the oscillator is small compared to the evanescent decay length $1/\kappa_\perp$ of the evanescent field and the same holds for the transverse dimensions of the oscillator, so that the electric field is assumed to be constant everywhere inside the integration volume. Thus, by linearizing $\vec{E}(\vec{r})$ about the equilibrium position of the nanoresonator and comparing the Hamiltonians (32) and (17) using (40), we find for the opto-mechanical coupling rate,

$$G_0 \approx 3.0\frac{\omega_\mathrm{c}\alpha_{||}\kappa_\perp L_\mathrm{tube}\xi^2}{n_\mathrm{c}^2\epsilon_0 V_\mathrm{mode}}\mathrm{e}^{-2\kappa_\perp d}C_\mathrm{corr}\,. \tag{41}$$

Here, we neglected the contribution of the perpendicular polarizability since, for carbon nanotubes, the perpendicular polarizability is typically one order of magnitude smaller than the parallel one. The geometry of the setup we consider here is illustrated in figure 3 and the dependence of alignment and positioning of the nanotube is accounted for in the correction factor C_corr. For a $\mathrm{TE}_{0,n}$-mode of the cavity field, the electric field is directed along $\hat{\varphi}$, i.e. tangential to the cavity rim, while the nanotube is aligned along $\vec{e}_\mathrm{nt} = \cos\theta'\hat{z} + \sin\theta'\hat{y}$. In addition, the deflection of the tube is not aligned with the electric field gradient. The direction of the deflection and the direction of the field gradient are given by $\vec{e}_\mathrm{osc} = \cos\theta'\hat{y} - \sin\theta'\hat{z}$ and $\hat{r} = \cos\varphi\hat{x} + \sin\varphi\hat{y}$. Finally, if d is the distance of the chip to the cavity rim, the actual distance of the oscillator to the rim is $d' = (a_\mathrm{c} + d)/\cos\varphi - a_\mathrm{c}$. Taking together all these corrections, we find for the correction factor $C_\mathrm{corr} \approx \mathrm{e}^{-2\kappa_\perp(d+a_\mathrm{c})(\sec\varphi-1)}\sin^2\theta'\cos\theta'\cos^2\varphi\sin\varphi$. This correction factor is maximized for $\sin^2\theta'_* = 2/3$ and $\varphi_* \approx 1/\sqrt{2\kappa_\perp(d+a_\mathrm{c})}$, resulting in $1/C_\mathrm{corr} \approx 15.5$ for a refracting index $n_\mathrm{c} = 1.44$.

10. Cavity losses induced by metallic nanotube electrodes

Preparing a nonclassical steady state demands a high-Q optical cavity as the linewidth κ needs to be comparable to the mechanical nonlinearity λ. Using conventional metallic electrodes for the mechanical frequency softening can potentially increase the cavity losses. To achieve the necessary low losses it is crucial to have deep subwavelength transverse dimensions for the electrodes.

We now give an estimate of the photon losses that may be induced by such electrodes and show that these are negligible. To do so, we model the electrodes as metallic cylinders and assume that their radius is much smaller than the wavelength of the evanescent cavity field. We assume the electrodes to be parallel to the waveguide, with a small misalignment angle θ. For the considered $\mathrm{TE}_{0,n}$ modes, the losses result from the misalignment only, as for $\theta = 0$ there is no field along the electrode axis. The resulting finesse $\mathcal{F}$ for the cavity is composed of the finesses $\mathcal{F}_i$ associated to the different decay channels, which by assuming independent loss channels reads

$$\frac{1}{\mathcal{F}} = \sum_i \frac{1}{\mathcal{F}_i}\,. \tag{42}$$

For each loss channel, the finesse $\mathcal{F}_i$ is determined by the ratio of the incident power and the fraction of power that it lost through the respective channel. The loss channels that will be considered subsequently are (1) scattering by the “bulk” of the electrodes modelled as a single metallic cylinder , (2) scattering by the “gap” between the electrodes and (3) absorbtion.

10.1. Incident field and incident power

For our calculations, we introduce new cylindrical co-ordinates (r', φ', z') for the electrode with the z-direction along the cylinder axis. We first express the field that is incident on the electrode in the electrode coordinates. The result will later be used to determine the scattered and absorbed fractions of the incident power.

To express the incident field on the electrodes in the electrode coordinates, we consider the projection of the electric field vector on the electrode axis (see FIG. 7) and assume that the field is constant over the electrode cross section with dimension $R \ll \kappa_\perp^{-1}$. This yields

$$E_{z'}^{(\mathrm{in})}(z') = \hat{z}' \cdot \hat{\varphi} E_\varphi \big|_{r'=0}\,. \tag{43}$$

We only need to determine the parallel field component $E_{z'}^{(\mathrm{in})}(z')$ here, as the other components in the relevant scattering field modes are then already completely determined by the wave equations for the field at the electrode. The origin of the primed axis lies at $(-d - a_\mathrm{c}, 0, 0)$ and the directions translate as

$$\hat{z}' = \sin\theta \hat{y} + \cos\theta \hat{z} \tag{44}$$

$$\hat{\varphi} = -\sin\varphi \hat{x} + \cos\varphi \hat{y}\,. \tag{45}$$

For points on the z'-axis we have

$$\cos\varphi = \frac{d + a_\mathrm{c}}{r}\,, \tag{46}$$

$$r = \sqrt{(d + a_\mathrm{c})^2 + z'^2 \sin^2\theta}\,, \tag{47}$$

$$z = z' \cos\theta\,. \tag{48}$$

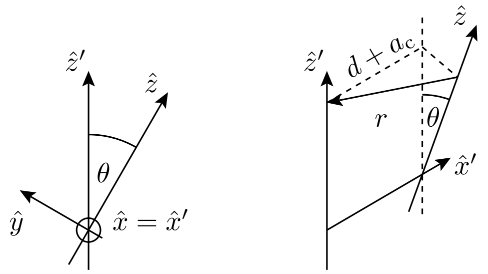

Figure 7. Relative alignment of electrode coordinates (r, φ, z) and waveguide coordinates (r', φ', z'). The misalignment is measured by a small angle θ.

For our further calculations it is convenient to express the incident field via its Fourier transform $E_{z'}^{(\mathrm{in})}(k') = \int_{-\infty}^{\infty} E_{z'}^{(\mathrm{in})}(z') \mathrm{e}^{-\mathrm{i}k'z'} \mathrm{d}z'$. Using this and equations (44)-(48) in (43) and (39) we can express the incident field as

$$E_{z'}^{(\mathrm{in})}(k') = \frac{-\mathrm{i}\omega}{\kappa_\perp} \sqrt{a_\mathrm{c}(d + a_\mathrm{c})} \tilde{\xi} \mathrm{e}^{-\kappa_\perp d} B_z(0) \underbrace{\int_{-\infty}^{\infty} \mathrm{d}x \frac{\mathrm{e}^{-\kappa_\perp (d + a_\mathrm{c})(\sqrt{1+x^2} - 1 + \mathrm{i}\tilde{k}x)}}{(1 + x^2)^{3/4}}}_{F} , \tag{49}$$

where we have substituted $x = z' \sin\theta / (d + a_\mathrm{c})$ and $\tilde{k} = (k' - n_\mathrm{c} k \cos\theta)/(\kappa_\perp \sin\theta)$. One can find an approximation for the integral F by applying the method of steepest descents, using $\kappa_\perp (d + a_\mathrm{c}) \gg 1$ and $d \sim \kappa_\perp^{-1} \ll a_\mathrm{c}$, which yields $|F| \approx \sqrt{2\pi/(d + a_\mathrm{c})\kappa_\perp} \mathrm{e}^{-\kappa_\perp (d + a_\mathrm{c}) |\tilde{k}|}$ for $|\theta| \ll 1$ and is maximized by $k' = k$ for small angles. Finally, we want to estimate the incident power, which is given by

$$P_\mathrm{I} = \int \mathrm{d}A \cdot |S| = \frac{2\pi n_\mathrm{c} c}{\mu_0} \left(\frac{k}{\gamma}\right)^2 |B_z(0)|^2 \int_0^{a_\mathrm{c}} r J_1^2(\gamma r) \mathrm{d}r \approx 0.51 \frac{c n_\mathrm{c}}{\mu_0} \left(\frac{k a_\mathrm{c}}{\gamma}\right)^2 |B_z(0)|^2 , \tag{50}$$

where we have used the Poynting vector $S = E_\varphi^* B_r / \mu_0$ with the vacuum permeability μ_0. Now that the incident fields are formulated, we continue to calculate scattering and absorption losses.

10.2. Scattering losses

We estimate an upper bound for the scattering losses by modelling the electrodes as perfectly conducting cylinders, as this maximizes the scattering. We expand the scattered field into solutions of the wave equation in cylindrical coordinates for the electrode. As the radius of the electrode R is much smaller than the wavelength of the incident field λ, all contributions are supressed like $(R/\lambda)^4$, as can be seen by a Taylor expansion of the corresponding cylindrical harmonics, except s-wave scattering of TM modes, for which the supression is only logarithmic. We further assume that the incident field is constant for a given cross section and determined by the field at the electrode's center. Moreover, we neglect multiple scattering between the electrode and the waveguide.

We determine the scattered field by use of the boundary condition $E_{z'}(r' = R, \varphi', z') = E_{z'}^{(\mathrm{in})} + E_{z'}^{(s)} = 0$ at the surface of the electrode. The transverse fields of TM solutions for the scattered field with z'-dependence $\exp(\mathrm{i}k'z')$ are given by

$$\vec{E}_{\perp}^{(s)} = \mathrm{i}\frac{k'}{k^2 - k'^2}\nabla_{\perp} E_{z'}^{(s)} \,, \tag{51}$$

$$\vec{H}_{\perp}^{(s)} = c\epsilon_0 \frac{k}{k'}\hat{z}' \times \vec{E}_{\perp}^{(s)} \,, \tag{52}$$

where k is the wave vector in vacuum and $E_{z'}^{(s)}(k') = H_0^{(1)}(\kappa_\perp r')\mathrm{e}^{\mathrm{i}k'z'}$, with $\kappa_\perp^2 = k^2 - k'^2$ and $k'^2 < k^2$. For $k'^2 > k^2$ the solution is evanescent and does not contribute the scattered power. Thus the scattered field can be written

$$E_{z'}^{(s)}(r', \varphi', z') \approx -\int_{-k}^{k} \frac{\mathrm{d}k'}{2\pi} E_{z'}^{(\mathrm{in})}(k') \frac{H_0^{(1)}(\sqrt{k^2 - k'^2}\,r')}{\mathrm{i}\frac{2}{\pi}\ln\left(\sqrt{k^2 - k'^2}R\right)} \mathrm{e}^{ik'z'} \,, \tag{53}$$

where $E_{z'}^{(\mathrm{in})}(k')$ is the Fourier transform of the incident field $E_{z'}^{(\mathrm{in})}(k')$ and where we have used the approximation $H_0^{(1)}(x) \approx \mathrm{i}\frac{2}{\pi}\ln x$ for $x \ll 1$. We calculate the scattered power by integrating the scattered energy flux across a cylinder with infinite radius $R_* \to \infty$ that enwraps the electrode, where we use $\langle \hat{r}' \cdot \vec{S} \rangle = \frac{1}{2}\Re\{\hat{r}' \cdot (\vec{E} \times \vec{H})\} = \frac{1}{2}\Re\{\frac{\mathrm{i}c\epsilon_0 k}{k'^2 - k^2}\frac{\partial E_{z'}^{(s)}}{\partial r'} E_{z'}^{(s)*}\}$, as well as $H_0^{(1)}(x) \approx \sqrt{2/\pi x}\exp\left[\mathrm{i}(x - \pi/4)\right]$ for $x \gg 1$. Thus the scattered power reads

$$\begin{aligned}
P_\mathrm{s} &\approx \frac{\pi}{4} c\epsilon_0 \int_{-k}^{k} \mathrm{d}k' \frac{k\left|E_{z'}^{(\mathrm{in})}(k')\right|^2}{(k^2 - k'^2)\ln^2(\sqrt{k^2 - k'^2})R} \\
&\lesssim \pi c\epsilon_0 \max\left\{\left|E_{z'}^{(\mathrm{in})}(k')\right|^2\right\}\Big|_{|k'| \le k} \underbrace{2\int_0^k \mathrm{d}k' \frac{k}{(k^2 - k'^2)\ln^2\left[(k^2 - k'^2)R^2\right]}}_{G}
\end{aligned}$$

The Integral G can be estimated for $kR \ll 1$ which yields $G \approx 1/(2|\ln(2kR)|)$. So by comparing this to the incident power (50) and using $\sin\theta \approx \theta$, $\cos\theta \approx 1$ for $|\theta| \ll 1$, we find an lower bound for the finesse associated to scattering losses

$$\mathcal{F}_\mathrm{s} \gtrsim \frac{2\mathrm{e}n_\mathrm{c}\sqrt{n_\mathrm{c}^2 - 1}}{\pi\xi^2} \ln\left(\frac{\lambda}{4\pi R}\right) \mathrm{e}^{4\pi\frac{n_\mathrm{c} - 1}{|\theta|}} \,. \tag{54}$$

Here we have introduced the denhancement factor $\xi = \frac{\gamma}{\kappa_\perp}\tilde{\xi}$ and assumed $d = 1/(2\kappa_\perp)$ and $a_\mathrm{c} = \lambda$. These assumptions are justified since for typical parameters one has $d \ll a_\mathrm{c}$ and $a_\mathrm{c} \sim \lambda$. For $\lambda = 1.55\,\mu\mathrm{m}$, $R = 10\,\mathrm{nm}$, $n_\mathrm{c} = 1.44$ and $\theta < 10^\circ$ we thus find $\mathcal{F}_\mathrm{s} > 7 \times 10^{15}$. Hence losses due to scattering are cleary sufficiently suppressed for electrodes of sub wave length radius that are aligned with $\theta < 10^\circ$ with the cavity rim.

10.3. Gap contribution to scattering losses

So far we have considered scattering from one single continuous electrode. Actually, our setup comprises two electrodes (see FIG. 3), separated by a gap in which the nanomechanical oscillator is positioned. We now estimate an upper bound to the additional losses that this gap may induce. To do so we model the gap of size D as a radiating dipole that is induced by the incident field. We approximate this dipole by a perfectly conducting sphere with radius $D/2$ to optain an upper bound for the induced diplole. Thus we find $p \sim \frac{\pi}{2}\epsilon_0 D^3 E^{(\mathrm{in})}_{\varphi'} \cos\theta'_*$ [42] and for the scattered power,

$$P_{\mathrm{g}} \lesssim \frac{\pi}{48}\epsilon_0 c k^4 D^6 \left(\frac{\omega\xi}{\gamma}|B_z(0)|\right)^2 \mathrm{e}^{-2\kappa_\perp d'} \cos^2\theta'_* \,. \tag{55}$$

Along the same lines as before, using (50), the associated finesse reads

$$\mathcal{F}_{\mathrm{g}} \gtrsim \frac{9}{\pi^5}\frac{n_{\mathrm{c}} a_{\mathrm{c}}^2 \lambda^4}{D^6 \zeta^2} \mathrm{e}^{2\kappa_\perp d'} \approx 3\times 10^{10} \,, \tag{56}$$

and shows that scattering losses due to the gap between both electrodes are negligible.

10.4. Absorption losses

We consider transparent electrodes with 2D conductivity σ that absorb the power

$$P_{\mathrm{a}} = \frac{1}{2}\int_{-\infty}^{\infty} \mathrm{d}z' \Re\left\{ I^* E^{(\mathrm{in})}_{z'} \right\} \,, \tag{57}$$

since $E^{(\mathrm{in})}_{z'}$ induces a current $I = 2\pi R\sigma E^{(\mathrm{in})}_{z'}$ in the electrode. By use of (43) and (50) the absorbed power reads

$$P_{\mathrm{a}} \approx \pi R \sigma \frac{\omega^2}{\gamma}\xi^2 a_{\mathrm{c}} \sin\theta \mathrm{e}^{-2\kappa_\perp d} |B_z(0)|^2 \underbrace{\int_{-\infty}^{\infty} \mathrm{d}x \frac{\mathrm{e}^{-2\kappa_\perp (d+a_{\mathrm{c}})(\sqrt{1+x^2}-1)}}{(1+x^2)^{3/2}}}_{J} \tag{58}$$

where we have again substituted $x = z'\sin\theta/(d+a_{\mathrm{c}})$ and $J \approx (\kappa_\perp(d+a_{\mathrm{c}})/\pi)^{-1/2}$ for $2\kappa_\perp(d+a_{\mathrm{c}}) \gg 1$. Thus using $d \ll a_{\mathrm{c}}$ yields for the finesse associated to absorption $\frac{1}{\mathcal{F}_{\mathrm{a}}} \approx \frac{\pi\sigma R\xi^2}{n_{\mathrm{c}} c \epsilon_0 a_{\mathrm{c}}}\sqrt{\frac{\pi}{\kappa_\perp a_{\mathrm{c}}}} \mathrm{e}^{-2\kappa_\perp d}\sin\theta$. Nanotubes exhibit an upper bound in the conductivity $\sigma_{\max} = 8\mathrm{e}^2/\mathrm{h}$ [43]. By assuming an off-resonant $\sigma = \tilde{\sigma}\sigma_{\max}$ with $\tilde{\sigma} < 1$, we get

$$\mathcal{F}_{\mathrm{a}} \gtrsim \frac{\mathrm{e}^{2\kappa_\perp d}}{16\pi\alpha_{\mathrm{F}}\xi^2\tilde{\sigma}}\sqrt{\frac{\kappa_\perp a_{\mathrm{c}}}{\pi}}\frac{n_{\mathrm{c}} a_{\mathrm{c}}}{R\sin\theta} \,, \tag{59}$$

with the fine structure constant $\alpha_{\mathrm{F}} \approx 1/137$. Plugging in the same values as before except that now $\theta < 3°$ and $R = 2.5$ nm and assuming $\tilde{\sigma} < 1/20$ we find $\mathcal{F}_{\mathrm{a}} \gtrsim 7\cdot 10^7$. Hence even though absorption losses clearly dominate over scattering losses, their effect can still be neglected for electrode radii $R < 3$ nm an alignment angles $\theta < 3°$.

11. Conclusions and Outlook

We have introduced a scheme to access a novel regime of optomechanics where the motion of the nanomechanical resonator becomes anharmonic and thus allows to explore genuine quantum dynamics. In our approach inhomogeneous electrostatic fields are applied to the nanomechanical resonator to enhance its anharmonicity per phonon until it becomes comparable to the linewidth of a high finesse optical cavity. An optomechanical coupling to driven modes of this high finesse cavity allows to selectively address transitions between phonon number states of the mechanical resonator and hence to control the mechanical motion at a Fock state resolved level. The scheme set forth thus opens new avenues for optomechanical manipulations of nanobeams, such as the preparation of phonon Fock states or optomechanically assisted approaches to the buckling instability [24, 25, 26].

12. Acknowledgements

This work is part of the Emmy Noether project HA 5593/1-1 and was supported the CRC 631, both funded by the German Science Foundation (DFG). IWR acknowledges support by the German Science Foundation (DFG) via the grant WI 3859/1-1 and Nanosystems Initiative Munich (NIM). The authors thank J. Kotthaus, T.J. Kippenberg, and A. Schliesser for enlightening discussions.

13. Appendix A

We consider the Liouvillian associated to the master equation (18) in the shifted representation (19)

$$\mathcal{L}(t) = \zeta^2 \mathcal{L}_0 + \zeta \mathcal{L}_1(\zeta^2 t) + \mathcal{L}_2(\zeta^2 t) \, , \tag{60}$$

where we have introduced a formal dimensionless parameter ζ that labels the different involved frequency scales and will later be used as a expansion parameter. After changing to an interaction picture for the mechanical mode (including the nonlinear part), the three parts of (60) read

$$\mathcal{L}_0 \rho = \sum_j \left\{ \mathrm{i} \left[\Delta_j a_j{}^\dagger a_j , \rho \right] + \frac{\kappa_j}{2} \mathcal{D}(a_j) \rho \right\} \, , \tag{61}$$

which describes the free cavity dynamics,

$$\mathcal{L}_1(\zeta^2 t) \rho = -\mathrm{i} \sum_{n,j} \frac{g_{\mathrm{m},j}}{\sqrt{2}} \left[\mathrm{e}^{\mathrm{i}\zeta^2 \delta_n t} \mathcal{L}^{(+)}_{1n,j} \rho + \mathrm{e}^{-\mathrm{i}\zeta^2 \delta_n t} \mathcal{L}^{(-)}_{1n,j} \rho \right] \, , \tag{62}$$

which describes the photon-phonon interaction, where $\mathcal{L}^{(+)}_{1n,j}\rho = \left[X_j b_n^\dagger , \rho \right]$, $\mathcal{L}^{(-)}_{1n,j}\rho = [X_j b_n , \rho]$ and with the cavity quadratures $X_j = \left(\alpha_j^* a_j + \alpha_j a_j{}^\dagger \right) / \sqrt{2} |\alpha_j|$, as well as

$$\mathcal{L}_2(\zeta^2 t) \rho = \frac{\gamma_\mathrm{m}}{2} \sum_{n,m} \left[(\overline{n} + 1) \mathrm{e}^{\mathrm{i}\lambda(n-m)\zeta^2 t} \mathcal{D}^-_{nm} \rho + \overline{n} \mathrm{e}^{-\mathrm{i}\lambda(n-m)\zeta^2 t} \mathcal{D}^+_{nm} \rho \right] , \tag{63}$$

which describes phonon dissipation with damping operators $\mathcal{D}^{-}_{nm}\rho = 2b_n\rho b^\dagger_m - b^\dagger_m b_n\rho - \rho b^\dagger_m b_n$, $\mathcal{D}^{+}_{nm}\rho = 2b^\dagger_n\rho b_m - b_m b^\dagger_n\rho - \rho b_m b^\dagger_n$. We now define projection operators

$$\mathcal{P}\rho = \mathrm{Tr}_{\mathrm{c}}\{\rho\} \otimes \rho^{(\mathrm{th})}_{\mathrm{c}}\,, \qquad \mathcal{Q} = \mathbb{1} - \mathcal{P}\,, \tag{64}$$

with the trace over all optical degrees of freedom of the cavities $\mathrm{Tr}_{\mathrm{c}}\{\rho\} = \mathrm{Tr}_{\mathrm{c},1}\dots\mathrm{Tr}_{\mathrm{c},j}\dots\{\rho\}$, and use thermal states for the cavity modes

$$\rho^{(\mathrm{th})}_{\mathrm{c}} = \bigotimes_j \rho^{(\mathrm{th})}_{\mathrm{c},j} \quad \text{with} \quad \rho^{(\mathrm{th})}_{\mathrm{c},j} = \frac{1}{n_{\mathrm{c},j}+1}\sum_{n=0}^{\infty}\left[\frac{n_{\mathrm{c},j}}{n_{\mathrm{c},j}+1}\right]^n |n\rangle\langle n|_{\mathrm{c},j}\,, \tag{65}$$

where $n_{\mathrm{c},j} = \overline{n}(\omega_j)$ is the Bose occupation number for the cavity mode with frequency ω_j. We will use $n_{\mathrm{c},j} = 0$ in the calculations, which is a excellent approximation for optical frequencies at cryogenic tempertures.

We derive coupled equations of motion for the relevant part $\mathcal{P}\rho$ and the irrelevant part $\mathcal{Q}\rho$, solve the irrelevant part formally and insert it into the relevant part to obtain a closed equation for the latter which reads

$$\mathcal{P}\dot{\rho} = \mathcal{P}\mathcal{L}(t)\mathcal{P}\rho + \mathcal{P}\mathcal{L}(t)\int_0^t \mathrm{d}\tau\mathcal{T}_+\left[\mathrm{e}^{\int_0^t \mathrm{d}\tau'\mathcal{Q}\mathcal{L}(\tau')\mathcal{Q}}\right]\mathcal{T}_-\left[\mathrm{e}^{-\int_0^\tau \mathrm{d}\tau''\mathcal{Q}\mathcal{L}(\tau'')\mathcal{Q}}\right]\mathcal{L}(\tau)\mathcal{P}\rho(\tau)\,. \tag{66}$$

As $\mathcal{P}\rho$ is a stationary state of $\mathcal{L}_0$ it follows that $\mathcal{L}_0\mathcal{P} = \mathcal{P}\mathcal{L}_0 = 0$. Furthermore we have $\mathcal{P}\mathcal{L}_2(\zeta^2 t) = \mathcal{L}_2(\zeta^2 t)\mathcal{P}$. We are looking for an expansion in $1/\zeta$ for $\zeta \gg 1$, so we can expand the time ordered terms to get

$$\mathcal{T}_+\left[\mathrm{e}^{\int_0^t \mathrm{d}\tau'\mathcal{Q}\mathcal{L}(\tau')\mathcal{Q}}\right]\mathcal{T}_-\left[\mathrm{e}^{-\int_0^\tau \mathrm{d}\tau''\mathcal{Q}\mathcal{L}(\tau'')\mathcal{Q}}\right] = \mathrm{e}^{\zeta^2\mathcal{Q}\mathcal{L}_0\mathcal{Q}(t-\tau)}\left[\mathbb{1} + \mathcal{O}\left(\frac{1}{\zeta}\right)\right]\,. \tag{67}$$

Using this and substituting $\tau' = \zeta^2(t-\tau)$, we arrive at

$$\mathcal{P}\dot{\rho} = \mathcal{P}\left[\zeta\mathcal{L}_1(\zeta^2 t) + \mathcal{L}_2(\zeta^2 t)\right]\mathcal{P}\rho + \mathcal{P}\mathcal{L}_1(\zeta^2 t)\mathcal{Q}\int_0^{\zeta^2 t}\mathrm{d}\tau'\mathrm{e}^{\mathcal{L}_0\tau'}\mathcal{Q}\mathcal{L}_1\left(\zeta^2 t - \tau'\right)\mathcal{P}\rho(t-\tau'/\zeta^2) + \mathcal{O}(1/\zeta^2)$$

To obtain now the lowest nontrivial order in $1/\zeta$ we apply the limit $\zeta \to \infty$. In this limit all fast rotating terms drop out which amounts to a RWA. Inserting (62) we get

$$\mathcal{P}\dot{\rho} = \mathcal{P}\mathcal{L}_2\mathcal{P}\rho + \sum_{n,i,j}\frac{|g_{\mathrm{m},j}|^2}{2}\left[\mathcal{P}\mathcal{L}^{(+)}_{1n,i}\int_0^\infty \mathrm{d}\tau'\mathrm{e}^{\mathrm{i}\delta_n\tau'}\mathrm{e}^{\mathcal{L}_0\tau'}\mathcal{Q}\mathcal{L}^{(-)}_{1n,j}\mathcal{P}\rho + \mathrm{H.\ c.}\right]\,, \tag{68}$$

If we now insert (62) and apply the projection (64) we obtain

$$\mathcal{P}\mathcal{L}^{(+)}_{1n,i}\mathcal{Q}\int_0^\infty \mathrm{d}\tau'\mathrm{e}^{(\mathrm{i}\delta_n+\mathcal{L}_0)\tau'}\mathcal{Q}\mathcal{L}^{(-)}_{1n,j}\mathcal{P}\rho = -\int_0^\infty \mathrm{d}\tau\mathrm{e}^{\mathrm{i}\delta_n\tau}\mathrm{Tr}_{\mathrm{c}}\left\{\left[X_i b^\dagger_n, \mathrm{e}^{\mathcal{L}_0\tau}\left[X_j b_n, \mu\otimes\rho^{(\mathrm{th})}_{\mathrm{c}}\right]\right]\right\}\,. \tag{69}$$

Here we have introduced the reduced density operator for the mechanical mode $\mu = \mathrm{Tr}_{\mathrm{c}}\left\{\rho\right\}$. The operators belonging to the mechanical mode can be pulled out of the trace, and so by defining the cavity correlation functions

$$G_j(\omega) = \delta_{ij} \int\limits_0^\infty \mathrm{d}\tau \mathrm{e}^{\mathrm{i}\omega\tau} \mathrm{Tr}_{\mathrm{c}} \left\{ X_i \mathrm{e}^{\mathcal{L}_0 \tau} X_j \rho_{\mathrm{c}}^{(\mathrm{th})} \right\} \,, \tag{70}$$

equation (68) becomes

$$\dot{\mu} = \mathcal{L}_2 \mu + \sum_{n,j} \frac{|g_{\mathrm{m},j}|^2}{2} \left\{ G_j(\delta_n) \left[b_n^\dagger, b_n \mu \right] - G_j^*(-\delta_n) \left[b_n^\dagger, \mu b_n \right] + \mathrm{H.c.} \right\} \,. \tag{71}$$

Note that there are no cross correlations between different cavity modes, which is expressed in the delta function δ_{ij}. The cavity two time correlations for each mode follow the dynamics of $\mathcal{L}_0$ and therefore

$$G_j(\omega) = \frac{1}{-2\mathrm{i}\left(\omega + \Delta_j\right) + \kappa_j} \,. \tag{72}$$

Rearranging (71) and switching back to Schrödinger picture yields the reduced master equation (22) with

$$A_{\pm,j}^n = \frac{g_{\mathrm{m},j}^2}{2} \Re\left\{ G_j(\mp\delta_n) \right\} \,, \quad \Delta_{\mathrm{m},j}^{n,\pm} = \frac{g_{\mathrm{m},j}^2}{2} \Im\left\{ G_j(\pm\delta_n) \right\} \,. \tag{73}$$

References

[1] T. Rocheleau, T. Ndukum, C. Macklin, J.B. Hertzberg, A.A. Clerk, and K.C. Schwab, Nature **463**, 72 (2010).

[2] A.D. O'Connell, M. Hofheinz, M. Ansmann, R.C. Bialczak, M. Lenander, E. Lucero, M. Neeley, D. Sank, H. Wang, M. Weides, J. Wenner, J.M. Martinis and A.N. Cleland, Nature **464**, 697 (2010).

[3] J.D. Teufel, T. Donner, Dale Li, J.H. Harlow, M.S. Allman, K. Cicak, A.J. Sirois, J.D. Whittaker, K.W. Lehnert, and R.W. Simmonds, Nature **475**, 359 (2011).

[4] J. Chan, T.P. Mayer Alegre, A.H. Safavi-Naeini, J.T. Hill, A. Krause, S. Gröblacher, M. Aspelmeyer, and O. Painter, Nature **478**, 89 (2011).

[5] T. J. Kippenberg and K. J. Vahala, Science **321**, 1172 (2008)

[6] A.D. Armour, M.P. Blencowe, and K.C. Schwab, Phys. Rev. Lett. **88**, 148301 (2002).

[7] F. Marquardt and S.M. Girvin, Physics **2**, 40 (2009).

[8] J.D. Teufel, T. Donner, M.A. Castellanos-Beltran, J.W. Harlow, and K.W. Lehnert, Nature Nanotech. **4**, 820 (2009).

[9] A. Schliesser, R. Riviére, G. Anetsberger, O. Arcizet, T.J. Kippenberg, Nat. Phys. **5**, 509 (2009).

[10] G. Anetsberger, E. Gavartin, O. Arcizet, Q.P. Unterreithmeier, E.M. Weig, M.L. Gorodetsky, J.P. Kotthaus, T.J. Kippenberg, Phys. Rev. A **82**, 061804 (2010).

[11] S.L. Adler and A. Bassi, Science **325**, 275 (2009).

[12] P. Ehrenfest, Z. Phys. A **45**, 455 (1927).

[13] P. Rabl, Phys. Rev. Lett. **107**, 063601 (2011).

[14] A. Nunnenkamp, K. Borkje, and S. M. Girvin, Phys. Rev. Lett. **107**, 063602 (2011).

[15] J. C. Sankey, C. Yang, B. M. Zwickl, A. M. Jayich and J. G. E. Harris, Nat. Phys. **6** 707 (2010)

[16] K. Jacobs, Phys. Rev. Lett. **99**, 117203 (2007).
[17] V. Peano and M. Thorwart, New J. Phys. **8**, 21 (2006).
[18] E. Babourina-Brooks, A. Doherty and G.J. Milburn, New J. Phys. **10**, 105020 (2008).
[19] I. Katz, A. Retzker, R. Straub, and R. Lifshitz, Phys. Rev. Lett. **99**, 040404 (2007).
[20] M.J. Hartmann and M.B. Plenio, Phys. Rev. Lett. **101**, 200503 (2008).
[21] Q.P. Unterreithmeier, E.M. Weig, and J.P. Kotthaus, Nature **458**, 1001 (2009).
[22] Wilson-Rae, I. and Nooshi, N. and Zwerger, W. and Kippenberg, T. J., Phys. Rev. Lett. **99**, 093901 (2007).
[23] F. Marquardt, J.P. Chen, A.A. Clerk, and S.M. Girvin, Phys. Rev. Lett. **99**, 093902 (2007).
[24] L.D. Landau and E.M. Lifshitz, *Theory of elasticity*, Pergamon, Oxford (1986).
[25] S.M. Carr, W.E. Lawrence, and M.N. Wybourne, Phys. Rev. B **64**, 220101 (2001).
[26] P. Werner and W. Zwerger, Europhys. Lett.**65** (2004).
[27] I. Wilson-Rae, N. Nooshi, J. Dobrindt, T.J. Kippenberg, and W. Zwerger, New J. Phys. **10**, 095007 (2008).
[28] H. P. Breuer and F. Petruccione, Oxford University Press (2002)
[29] G. Anetsberger, O. Arcizet, Q.P. Unterreithmeier, R. Riviére, A. Schliesser, E.M. Weig, J.P. Kotthaus, and T.J. Kippenberg, Nat. Phys. **5**, 909 (2009).
[30] M. Pöllinger, D. O'Shea, F. Warken and A. Rauschenbeutel, Phys. Rev. Lett. **103**, 053901 (2009).
[31] G.A. Steele, A.K. Hüttel, B. Witkamp, M. Poot, H.B. Meerwaldt, L.P. Kouwenhoven, and H.S.J. van der Zant, Science **325**, 1103 (2009).
[32] B. Lassagne, Y. Tarakanov, J. Kinaret, D. Garcia-Sanchez, and A. Bachtold, Science **325**, 1107 (2009).
[33] A.K. Hüttel, G.A. Steele, B. Witkamp, M. Poot, L.P. Kouwenhoven and H.S.J. van der Zant, Nano Lett. **9**, 2547 (2009).
[34] A. Eichler, J. Moser, J. Chaste, M. Zdrojek, I. Wilson-Rae, and A. Bachtold, Nature Nanotech. **6**, 339 (2011).
[35] Hofheinz, Max and Weig, E. M. and Ansmann, M. and Bialczak, Radoslaw C., Lucero, E., Neeley, M., O'Connell, A. D., Wang, H., Martinis, J. M., and Cleland, A. N., Nature **454**, 310 (2008).
[36] B. Kozinsky and N. Marzari, Phys. Rev. Lett. **96**, 166801 (2006).
[37] T. J. Kippenberg, S. M. Spillane, and K. J. Vahala, App. Phys. Lett. **85**, 6113 (2004)
[38] C. W. Gardiner and M. J. Collett, Phys. Rev. A **31**, 3761 (1985)
[39] D. Santamore, A.C. Doherty, and M.C. Cross, Phys. Rev. B **70**, 144301 (2004).
[40] A.M. Jayich, J.C. Sankey, B.M. Zwickl, C. Yang, J.D. Thompson, S.M. Girvin, A.A. Clerk, F. Marquardt, and J.G.E. Harris, New J. Phys. **10**, 095008 (2008).
[41] E. Buks, E. Arbel-Segev, S. Zaitsev, B. Abdo, and M.P. Blencowe, Europhys. Lett. **81**, 10001 (2008).
[42] J. D. Jackson, *Classical Electrodynamics*, Wiley, New York (1998)
[43] D.Y. Joh, J. Kinder, L.H. Herman, S.-Y. Ju, M.A. Segal, J.N. Johnson, G.K.-L. Chan and J. Park, Nature Nanotech. **6**, 51 (2011).